The effects of Hot Isostatic Pressing (HIP) and solubilization heat treatment on the density, mechanical properties and microstructure of austenitic stainless steel parts produced by Selective Laser Melting (SLM)

Erica Liverani[1], Adrian H. A. Lutey[2*], Alessandro Ascari[1], Alessandro Fortunato[1]

[1]*Dipartimento di Ingegneria Industriale (DIN), Università di Bologna, viale Risorgimento 2, Bologna, Italy*

[2]*Dipartimento di Ingegneria e Architettura, Università di Parma, parco Area delle Scienze 181/A, Parma, Italy*

*Corresponding author. Tel: +39 0521906029, email: *adrian.lutey@unipr.it*

ABSTRACT

Despite ongoing optimization, Selective Laser Melting (SLM) technology still cannot guarantee the production of completely defect-free components. This work investigates Hot Isostatic Pressing (HIP) in a nitrogen environment and solubilization heat treatment as methods for improving the quality of 316L stainless steel components produced by SLM. The characteristics of HIP-treated specimens are firstly correlated with the initial density of samples obtained with different SLM process parameters, showing that HIP is effective at eliminating pores in components with high initial density (above 99%) but not in those with low initial density (approximately 94%). Subsequently, the mechanical properties and microstructure of 316L stainless steel specimens produced by SLM are examined in the as-built state and after various post-process conditions including solubilization heat treatment and HIP at pressures from 50 bar to 2000 bar. The observed effects of post-processing on the porosity and microstructure of each specimen are consistent with hardness and tensile test results, with the benefits and limitations of HIP clarified for future implementation.

Keywords: Selective Laser Melting; Hot Isostatic Pressing; Additive Manufacturing; 316L Stainless Steel

1. Introduction

Powder-based additive manufacturing (AM) technologies are currently seeing strong development due to their potential to produce advanced components with improved functionality. The current state-of-the-art of polymer AM is mainly focused on introduction of innovative materials and complex 3D printed structures [1]. In contrast, there are still a number of technical shortfalls in relation to AM of metals due to the limited number of commercially available metal powders and the presence of defects. Uncontrolled porosity of up to 0.5 % is very common even with optimized process parameters [2], while the resulting physical properties dependent on process parameters [3]. The choice of parameters has a strong influence on the cooling rate and solidification mode, which in turn influence the resulting microstructure, mechanical properties [4] and machinability [5]. For materials such as aluminum alloys, metallurgical defects such as balling, porosity, residual stresses and oxidation can be difficult to control, thus limiting the number of materials suitable for Selective Laser Melting (SLM) [6]. Process optimization can also require a compromise between low porosity and high dimensional control depending on the applied energy density [7]. Though existing literature provides a solid technical basis and process parameter window for those wishing to apply SLM within new applications, this technology still cannot guarantee the production of completely defect-free components.

The presence of pores does not necessarily compromise static mechanical performance, with the mechanical strength obtained with SLM often greater than that obtained with traditional manufacturing methods [8-10]. Fatigue performance, however, exhibits strong dependence on density and pore dimensions [11-13]. Parts produced by SLM can display similar hardness to those produced with conventional methods but a significant reduction in fatigue strength even after machining to reduce the surface roughness [14]. For example, a reduction in fatigue limit from 640 MPa with conventional manufacturing to 300 MPa with SLM has been demonstrated for 17-4 PH stainless steel [15]. The presence of defects not only compromises the integrity of components subject to dynamic loading, but also has a negative influence on corrosion resistance. It has been shown that the breakdown potential of 316L stainless steel is lower for SLM parts than for the standard bulk material [16], with the former exhibiting greater susceptibility to pitting corrosion. This is an important aspect, as the applications of greatest interest for AISI 316L stainless steel are related to the material's compatibility with food products and biomedical substances. Both these fields have strict standards relating to surface quality that require complete absence of surface defects to avoid accumulation of material or buildup of bacteria, with parts often undergoing harsh washing or sterilization cycles.

Defects during AM can be minimized by employing specific laser scanning approaches. Multi-scanning strategies inducing re-melting have been shown to decrease porosity from 0.77 % to 0.036 % for 316L stainless steel [17] and from 0.39 % to 0.05 % for Ti-5Al-2.5Sn alloy [18]. Though it has been shown that this technique can be used to largely reduce porosity, defects are not completely eliminated and build time is significantly longer. An alternative is post-processing with Hot Isostatic Pressing (HIP). This technology has historically been utilized to compress sintered parts such as cutting tool inserts or to improve the integrity of cast components by reducing the presence of pores. HIP consists of simultaneously subjecting a component to elevated temperature and pressure within a chamber containing a (usually inert) gas, which compresses the component in an isostatic manner. This leads internal pores to collapse, entrapped gas to dissolve within the matrix and powder particles to consolidate within the rest of the structure [19]. HIP has seen limited application to AM to date, with literature mainly focusing on Nickel and Titanium alloys. Heat treatment and HIP performed on Inconel 625 SLM specimens have been shown to increase ductility and decrease strength, suggesting that optimization of post-processing is an important factor in achieving specific mechanical properties [20]. Increases in density from 99.917 % to 99.985 % following HIP post-processing have been demonstrated for Inconel 718 SLM specimens [21]. It has also been shown that the fatigue life of Ti-6Al-4V SLM specimens improves with HIP post-processing due to a reduction in the defect population and changes in the microstructure surrounding defects [22]. In some cases, similar fatigue behavior to the wrought material has been achieved [23]. In a recent study by Lavery *et al.* [24] investigating the density and mechanical properties of 316L stainless steel specimens following HIP, it was shown that it is possible to reduce the presence of pores significantly. The authors did not, however, vary post-processing parameters and therefore did not fully exploit the link between SLM and HIP. Finally, Roettger *et al.* [25] performed solution annealing and HIP on 316L stainless steel SLM specimens in an argon environment. They found that argon gas pores could not be sufficiently removed with subsequent heat treatment due to insolubility of argon within the steel matrix.

The aim of the present work is therefore to investigate the effects of solubilization heat treatment and HIP performed in a nitrogen environment at different pressures on the mechanical strength, hardness and microstructure of 316L stainless steel samples produced by SLM. To do this, the relationship between initial porosity and post-HIP density is first examined to determine whether full optimization of SLM is necessary to obtain defect-free final components. Subsequently, the effects of HIP at 1150 °C on the mechanical properties and microstructure are examined while varying the pressure up to 2000 bar. To complete the investigation, the effects of solubilization heat treatment on as-built and HIP post-processed samples are also explored. The investigation confirms that correct SLM parameter optimization is always necessary to obtain defect-free components, while providing insight into the range of mechanical properties and microstructures that can be obtained with solubilization heat treatment and HIP post-processing.

2. Materials and methods

2.1 Sample production

Atomized 316L stainless steel powder supplied by LPW® with nominal particle size in the range 15-45 μm was used to produce all samples for experiments. The nominal chemical composition of this powder is reported in Table 1. Samples were produced by SLM with a MYSINT100 machine.

Table 1 Nominal chemical composition of AISI 316L steel powder used for experiments [wt. %]

Cr	Mn	Si	C	P	S	Mo	Ni	Fe
17.5-18	≤ 2	≤ 0.75	≤ 0.3	≤0.025	≤0.01	2.25-2.5	12.5-13	Bal.

All samples were built in a nitrogen environment with a residual oxygen content of 0.2 vol%. Process parameters, scanning strategy, build orientation and supporting structures were defined within the Autofab software. A rotating 3 × 3 mm^2 chessboard scanning strategy was utilized to melt the bulk volume, with an alternating parallel-line laser scanning strategy applied within each square with a hatch spacing of 0.06 mm.

A first experimental campaign denoted the "density test" (DT) focused on the link between the initial porosity obtained with a specific set of SLM process parameters and the final porosity obtained after HIP. During this phase, an equal number of SLM samples with low density (LD) and high density (HD) were produced based on process parameters derived in a previous study [8]. For this purpose, 26 samples (13 LD and 13 HD) of diameter 12 mm and height 15 mm were produced with the parameters given in Table 2. The layer thickness was set to 20 µm in all cases.

Table 2 SLM process parameters used in the DT experimental campaign

Type	Power [W]	Scanning speed [mm/s]	Energy density [J/mm^3]
Low density [LD]	70	1200	48
High density [HD]	130	700	155

After production, the density of all samples was measured using Archimedes' principle. This non-destructive technique allowed the density of each sample to be measured before and after HIP post-processing. One sample from each set of parameters, denoted LD$_{ref}$ and HD$_{ref}$, was instead sectioned to allow measurement of the density with image processing. Samples were then divided into separate groups and subject to HIP. Process parameters are given in Table 3. Three LD and three HD samples were treated for each set of HIP parameters.

Table 3 HIP parameters used in the DT experimental campaign

	Temperature [°C]	Pressure [bar]	Time [h]
HIP$_{50}$	1150	50	3
HIP$_{1050}$		1050	
HIP$_{1500}$		1500	
HIP$_{2000}$		2000	

Once the relationship between the initial porosity obtained with SLM and the final porosity obtained with HIP had been defined, the investigation focused on evaluating the mechanical properties and microstructure of components subject to different post-processing cycles. Within this second experimental campaign denoted the "mechanical and microstructural test" (MMT), only HD specimens were considered as it had been found that HIP did not increase the density of LD specimens sufficiently to be of interest. Twenty-four tensile test specimens with geometry in line with UNI ISO 6892-1 were produced by SLM during the MMT experimental campaign. These were then subject to post-processing with the conditions given in Table 4.

A typical solubilization heat treatment was selected for austenitic stainless steel consisting of heating to 1050 °C in a nitrogen environment and maintaining at this temperature for 30 minutes before rapidly cooling in water. A schematic representation of the entire experimental procedure is given in Fig. 1.

Table 4 Post-processing conditions for the MMT experimental campaign

No. of tested samples	Post-process
4	None
4	HIP_{50}
4	HIP_{1050}
4	HIP_{2000}
4	Solubilization
4	HIP_{1050} + Solubilization

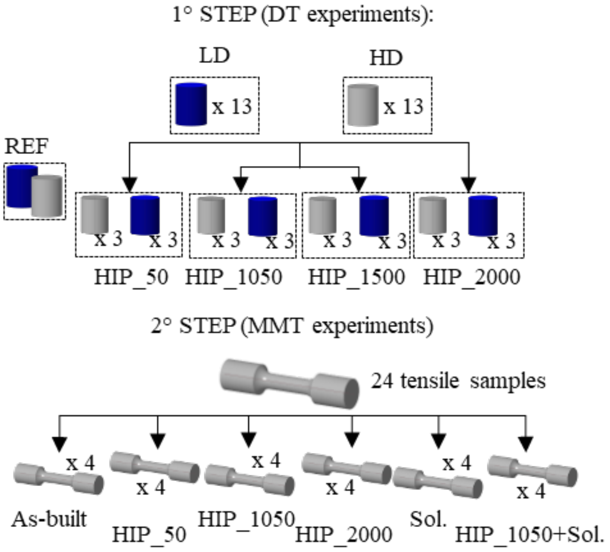

Fig 1 Schematic representation of entire experimental campaign

2.2 Density measurements

A non-destructive test was employed to evaluate the density of all samples. A PS600 R2 Radwag balance with a density measurement device for solid materials and a measurement accuracy of 0.001 g was used to perform density measurements using Archimedes' principle. This approach consists of weighing the component in air and in distilled water at room temperature. The ratio of the difference in weight in water and in air is equal to the density of the component, noting that the density of water is 1 g/cm^3. Though this technique is highly precise, it does not account for surface pores where water can enter. Such a limitation was considered negligible in the present case due to the fact that HIP is not able to close external pores. As such, comparison of the measured density before and after HIP remains coherent.

Image processing was employed to measure the density of selected samples based on cross-sections taken orthogonally to the SLM build plane. Two samples were mounted in epoxy resin, ground and polished. They were then analyzed with an optical microscope without chemical etching. The resulting images were processed with the software ImageJ to determine the density of each sample based on the area ratio of pores within the section.

2.3 Mechanical characterization

The influence of post-processing conditions on the mechanical properties of each sample was determined with tensile tests. Experiments were carried out in line with ISO 6892-1 on circular specimens with a diameter of 6 mm using an Instrom hydraulic testing machine with 100 kN load cell and 17 mm gauge length extensometer. Specimens were machined to the required geometry to minimize the effects of surface defects. The strain rate was maintained constant at 10^{-3} s^{-1} using a cross-head separation rate of 1 mm/min.

Representative as-built and treated samples were then cut from both grip regions of each tensile test specimen and prepared in line with standard metallographic procedures. Density measurements were repeated with image processing to verify previously obtained data. Hardness tests were then performed with a Vickers micro-hardness device (Remet, HX-1000) based on at least six indentations with a load of 1000 g. Hardness measurements were performed on samples cut from both grip regions of each tensile test specimen to determine possible differences between the two as a result of variations in thermal cycle with position during SLM production.

2.4 Microstructural analysis

Polished samples obtained during the DT experimental campaign and those obtained from tensile test specimens during the MMT experimental campaign were chemically etched with Vilella's reagent to reveal their microstructures. Optical microscopy (OM) was then performed with a Nikon optical microscope with a magnification of 5-50×. Following OM, the cross-sections of tensile test specimens were analyzed with scanning electron microscopy (SEM) to determine the presence and types of defects within each sample and evaluate the presence of critical phases such as oxides or carbides. Energy dispersive spectroscopy (EDS, X-Act/INCA, Oxford Instruments) was then used to analyze the chemical composition of each sample.

3. Results

3.1 Density

The density of all 26 cylinders produced during the DT experimental campaign was measured both immediately after SLM production and again after HIP post-processing. Initial average density values for as-built samples are summarized in Table 5. Percentage values were determined based on a reference density of 7.93 g/cm^3, which was chosen to achieve closest alignment between data obtained using Archimedes' principle and that obtained using image processing for the LD_{ref} and HD_{ref} samples. Images used for the latter, presented in Fig. 2, were obtained by combining microscope images acquired with a magnification of 2× and subsequently processing and analyzing the results with the software Image J.

Percentage density values therefore had the scope of making comparison between measured data more straightforward, while only density values in [g/cm^3] were to be considered as absolute values.

Table 5 Density of as-built DT samples obtained using Archimedes' principle

	Density [g/cm^3]	Density [%]
LD (mean)	7.43	93.73
HD (mean)	7.92	99.81
LD$_{ref}$	7.46	94.07
HD$_{ref}$	7.91	99.75

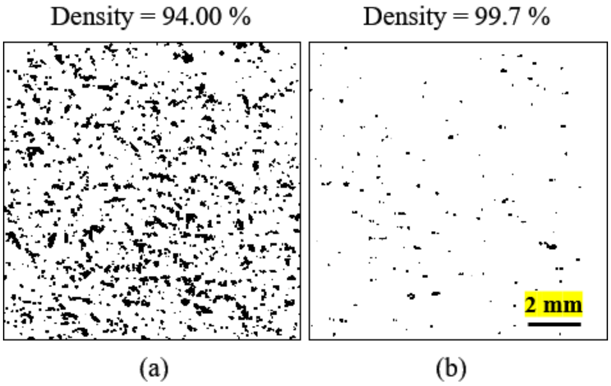

Fig 2 Density obtained with OM image processing for **a** LD$_{ref}$ and **b** HD$_{ref}$ samples

Once the density of the as-built samples had been determined, they were divided into groups of three and subject to HIP at various pressures (Table 3). The density of all samples was then measured again. The initial and final density of all tested samples is shown in Fig. 3. The presented data are averages of three samples for each type, subdivided into initial process parameters (LD and HD) and HIP pressure (50, 1050, 1550 and 2000 bar).

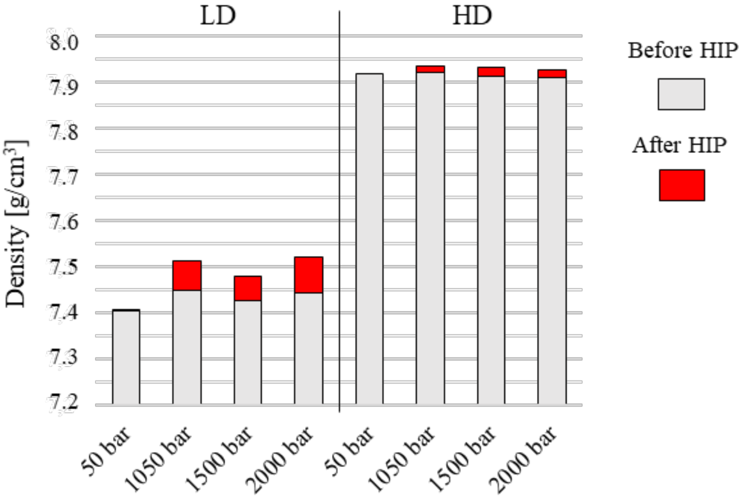

Fig 3 Comparison of density before and after HIP

Upon examination of Fig. 3, it is possible to note the following:

1) Samples with lower initial density (LD) exhibit a larger increase in density after HIP;

2) The density of LD samples after HIP nonetheless remains very low (see also Fig. 4);

3) A pressure of 50 bar has no influence on sample density;

4) Increasing the HIP pressure from 1050 bar to 2000 bar achieves no further increases in density, both in the case of LD and HD samples. This implies that an asymptote exists above which further increases in pressure provide no significant gains in terms of reducing porosity.

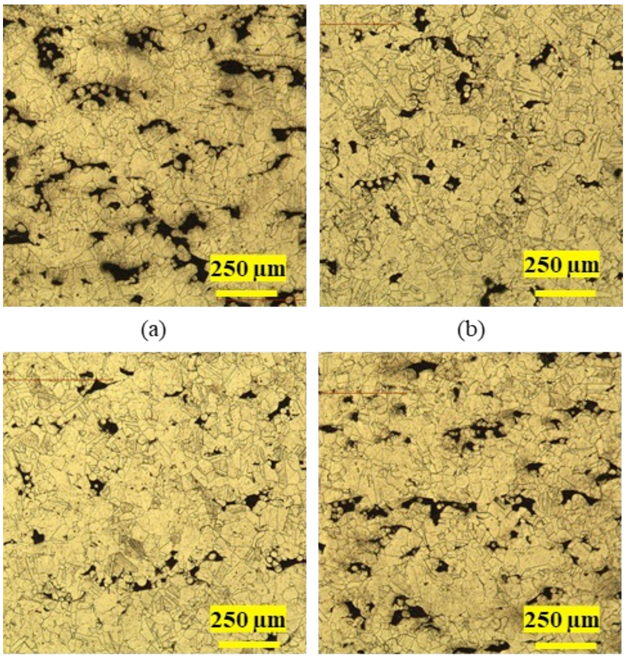

(a) (b) (c) (d)

Fig 4 Micrographs of LD samples after HIP at **a** 50 bar, **b** 1050 bar, **c** 1500 bar and **d** 2000 bar

To verify the density obtained using Archimedes' principle, one HD sample for each set of HIP parameters was also measured with OM image processing (Fig. 5). The obtained density values, presented in Table 6, are coherent with the preceding observations.

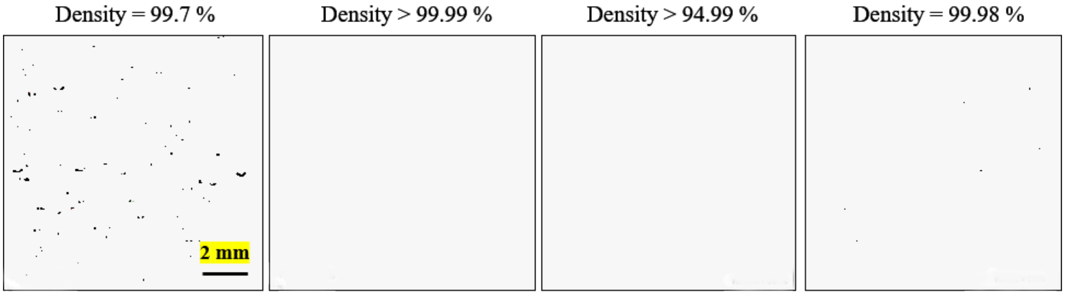

(a) (b) (c) (d)

Fig 5 OM images and analysis of HD samples after HIP at **a** 50 bar, **b** 1050 bar, **c** 1500 bar and **d** 2000 bar

Table 6 Density of HD samples obtained with image processing after HIP at various pressures

	50 bar	1050 bar	1500 bar	2000 bar
Density [%]	99.71	> 99.99	> 99.99	99.98

Results obtained during this first experimental campaign (DT) confirmed well-known outcomes in relation to HIP post-processing of cast components; that is, that the mechanism with which pores collapse under the action of high pressure and temperature during HIP is a combination of plastic deformation and subsequent welding of pores via diffusion of atoms. In this way, pores of small dimensions dissolve into the matrix while large pores reduce in size. There is no specific discussion within the literature as to whether a maximum percentage reduction in porosity exists for a given set of HIP processing parameters. It can nonetheless be deduced from the available data for cast components that initial porosity up to 1% can be almost completely eliminated via HIP [26,27], while components with initial porosity above 1% can never achieve full density. In [28], for example, the authors perform HIP post-processing on cast components with initial porosity between 2.6 – 6.9%, achieving relative reductions in porosity of no more than 20% in all cases. The situation is obvious quite different, however, where the raw material is in the form of powder and the final density after HIP processing is 100 % [29].

3.2 Mechanical properties and hardness

Results from the DT experimental campaign demonstrated that HIP post-processing was not capable of increasing the density to 100 % where the initial density was low (approximately 94 %), even with pressures up to 2000 bar. For the MMT experimental campaign, LD samples were therefore no longer considered. The DT campaign also highlighted the fact that increasing the HIP pressure from 1050 bar to 2000 bar had no significant effect on results. As such, a HIP pressure of 1500 bar was not considered for mechanical testing and microstructural analysis. Furthermore, as outlined in Section 2, a solubilization heat treatment was included amongst the post-processing conditions. Solubilization was tested both as a standalone process after SLM production and after HIP at 1050 bar (Table 4). All samples obtained in this way were subject to tensile tests (Fig. 6).

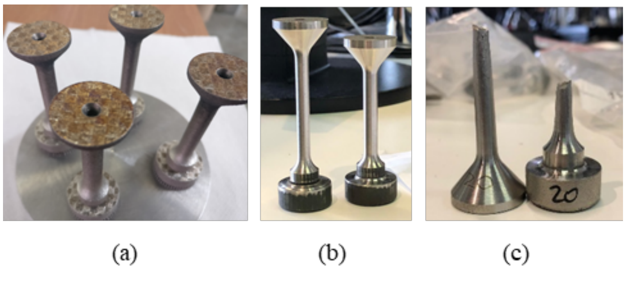

Figure 6: Tensile test specimens in **a** as-built condition, **b** after turning and **c** after tensile testing.

Results are displayed in Figs. 7 and 8. The average yield strength (YS), ultimate tensile strength (UTS) and elongation of all samples are presented in Fig. 7, together with the standard deviation of each. The mechanical characteristics are very evident and consistent, allowing the following observations to be made:

1) The UTS does not change appreciably with variations in post-processing conditions. Values remain close to 570 MPa, in line with reference values for the bulk material. The only exceptions are samples subject to solubilization heat treatment alone, leading to a lower UTS of approximately 540 MPa;
2) Highest YS is obtained with as-built specimens. Samples subject to HIP instead exhibit approximately 45% lower values. Those subject to solubilization heat treatment alone display intermediate behavior, with a YS of approximately 370 MPa;
3) The percentage elongation is much lower for as-built samples, which display lower ductility than post-processed specimens. Again, samples subject to the solubilization heat treatment alone display intermediate behavior;
4) In relation to the percentage elongation, samples subject to HIP post-processing at 50 bar display significant differences to those treated at higher pressures. At low pressure, the average elongation is 52.7 %, while values of up to 70 % are obtained with high HIP pressure.

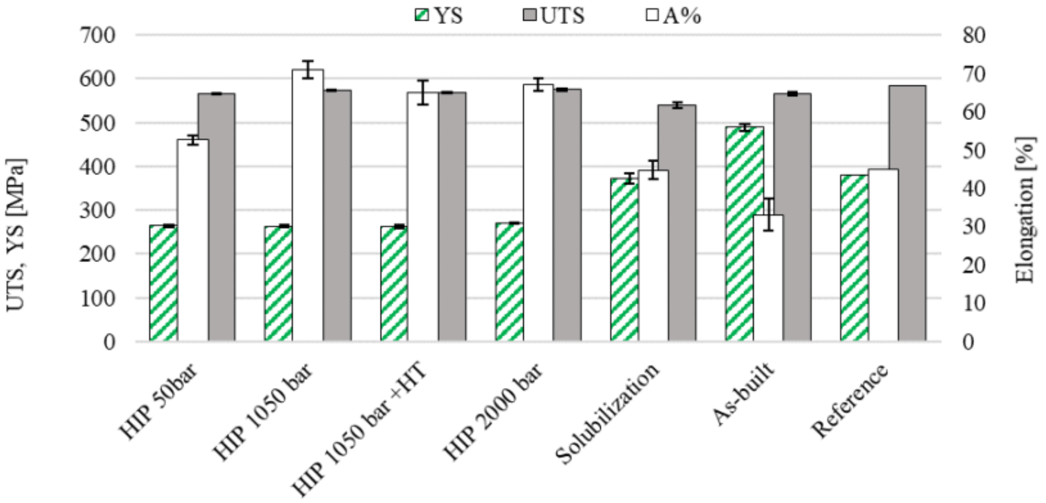

Fig 7 UTS, YS and elongation of all samples. Reference values refer to an annealed, cold-drawn bar [30]

Stress-strain diagrams of representative samples are displayed in Fig. 8. The as-built samples do not present significant strain hardening plastic behavior, while in all other cases this effect is evident, in particular for HIP samples. This strengthening occurs due to movement of dislocations within the crystal structure. Such contrasting behavior was confirmed with microstructural analysis and will be elaborated on below.

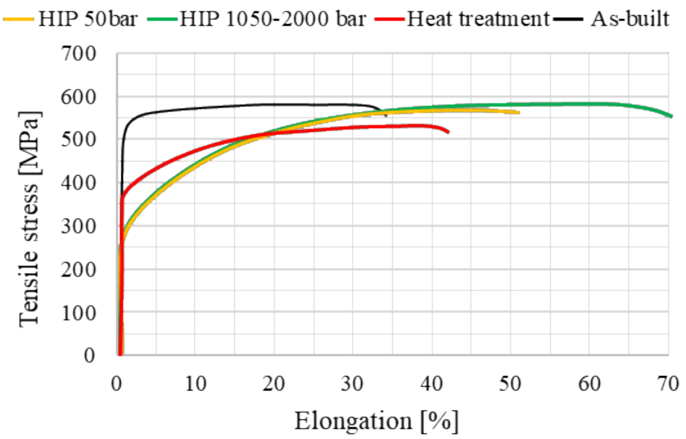

Fig 8 Stress-strain diagrams of representative samples

After tensile tests, representative as-built and post-processed samples were cut from both grip regions, mounted in resin and polished for micro-hardness tests. Hardness values presented in Table 7 are averages obtained with 6-8 indentations.

Table 7 Hardness of samples subject to various post-processing conditions

Post-process	Hardness 1000 g [HV]	
	Bottom	Top
None	242 ±11.7	242 ±3.3
HIP_{50}	158 ±10.5	166±10.5
HIP_{1050}	161 ±5.0	171 ±18.7
HIP_{2000}	159 ±9.6	186±17.4
Solubilization	194 ±11.7	191 ±5.9
HIP_{1050} + Solubilization	156 ±5.8	189±14.2

The following observations can be made in relation to these results:

1) The hardness of as-built samples does not vary with specimen height. This outcome is in contrast with some results presented in the literature [8]; however, it is important to note that such variations are related to the thermal cycle that the component is subject to, which in turn is related to both the geometry and number of specimens produced simultaneously [31]. In the present case, it is likely that the height (approximately 70 mm), combined with the geometry and number of samples (four per platform) led to negligible differences in the thermal cycle induced at the initial and final stages of printing.
2) The hardness of samples subject to HIP post-processing is lower than as-built samples. Negligible differences between each condition can be observed at the bottom of each sample, while hardness is considerably higher at the top and increases with pressure;
3) Solubilized samples are characterized by intermediate hardness, confirming observations relating to the yield strength obtained during tensile tests;
4) Results relating to samples solubilized after HIP suggest that differences in hardness between the top and bottom are primarily due to HIP. It is likely that a small temperature difference existed between the upper and lower parts of the autoclave in which HIP was

performed. This conclusion is based on the fact that solubilization on its own led to a homogeneous hardness profile, while such differences were only observed in samples first subject to HIP.

3.3 Chemical composition and microstructure

The chemical composition of each SLM sample before and after post processing was analyzed with SEM-EDS and compared to the powder composition provided by the supplier. Specimens subject to HIP at 1050 bar were chosen to provide representative values. The results of this analysis are presented in Table. 8 and are in approximate alignment with the initial nominal powder composition (Table 1).

Table 8 Chemical composition of SLM components before and after post processing [wt.%]

wt. %	Cr	Mn	Si	Mo	Ni	Fe
As-built	18.33	1.49	0.65	2.55	12.40	Bal.
Solubilized	18.44	1.53	0.62	2.45	12.20	Bal.
HIP at 1050 bar	17.58	1.37	0.57	2.22	11.96	Bal.

The microstructures of as-built samples presented in Fig. 9 are typical of SLM components. They are characterized by clearly visible melted zones in correspondence with each laser track. Fig. 9a displays a cross-section obtained parallel to the build direction in the *z*-*x* plane (see reference system in the left of the figure), showing melt-pools of adjacent layers. Fig. 9b instead corresponds to a cross-section obtained within a single layer in the *x*-*y* direction.

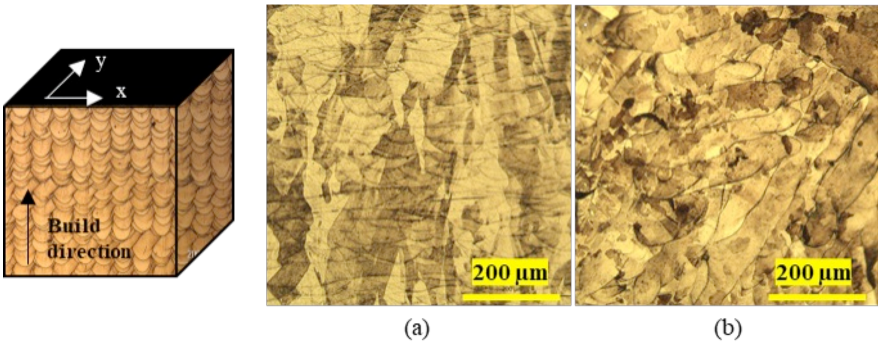

Fig 9 Microstructure of as-built specimens **a** parallel to the build direction and **b** within a single layer

SEM images of a representative as-built sample are displayed in Fig. 10. These confirm the presence of structures that are typically produced during SLM, including large grains within the fused zone and sub-micrometer cells with equiaxed (Fig.10a) or columnar (Fig.10b) geometry. The geometry of these cells depends primarily on the temperature gradient generated between the center of the melt pool and its boundaries. The lower temperature gradient and higher solidification rate at the center of the melt pool promote equiaxed grains, while opposite conditions at the perimeter of the melt pool favor formation of columnar grains [32].

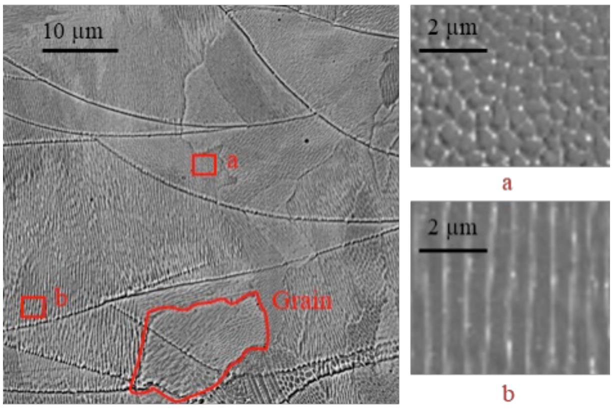

Fig 10 Microstructure of a representative as-built sample obtained by SEM

'Islands' of cells with larger dimensions (2-5 μm) were also observed, allowing the chemical composition of these structures and their boundaries to be studied. The results of this analysis are displayed in Fig. 11.

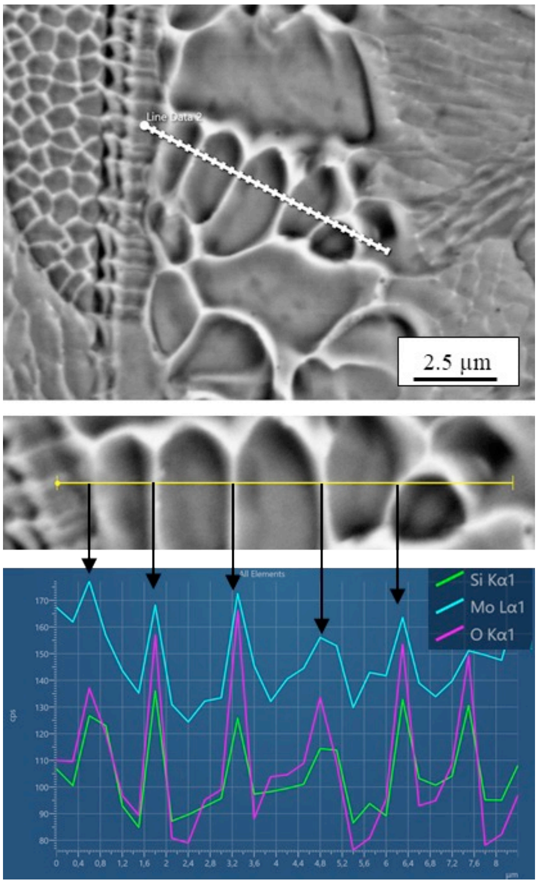

Fig 11 Chemical composition at cell boundaries

The distinct white color of crests in the SEM images with backscattering immediately highlights enrichment of heavy elements or phases at sub-grain boundaries. From line scan EDS measurements, it is clear that this heavy element is Mo. Precipitates are also generally rich in Si and O compared to matrix regions and thus may be attributed to silicon dioxide (e.g. "spectrum 3" in Table 9).

Zhong *et al.* [33] hypothesized that inter-granular segregation of Mo at cellular boundaries acts as a reinforcing element against crack propagation and therefore contributes to the increased strength of as-built SLM samples compared to those produced with conventional processes. This explanation is in line with the results of tensile tests obtained within the present work, where the yield strength of as-built and post-processed samples was much higher than the reference value (Fig. 7).

Detailed discussion of typical defects found during SEM analysis of as-built samples has already been provided in a previous work [8]. In the present study, no new characteristic cases were observed. Post-processing of samples instead led to modification of the microstructure, as can be seen in Figs. 12 and 13. With solubilization heat treatment only (Fig. 12), the dimensions and direction of grain growth do not appear to undergo significant changes. It is nonetheless evident that melt-pool boundaries disappear. Upon observation of the SEM images, it is also clear that sub-micrometric cells are no longer present. This behavior is in line with other works in the literature [34,35] showing that these cells begin to dissolve upon reaching a temperature of 900°C.

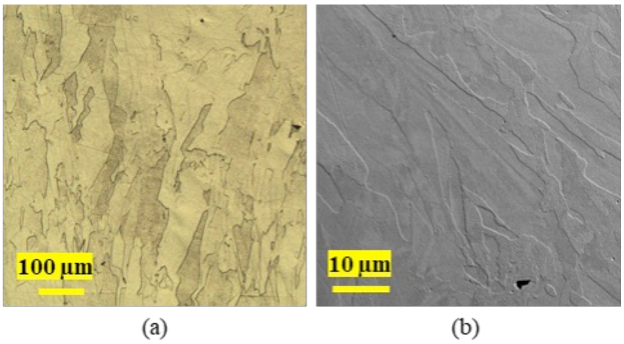

Fig 12 Microstructure of solubilized sample obtained with **a** OM and **b** SEM

The microstructure undergoes further modification during HIP, with complete recrystallization of the material and the appearance of twins. Figure 13 presents micrographs of samples subject to HIP at various pressures. With the exception of the lowest tested pressure (50 bar), there are no variations in microstructure or grain size with increasing pressure.

Localized dark regions along grain boundaries were further investigated with SEM. Two representative imagines are shown in Fig. 14. Irrespective of the pressure at which HIP was performed, all samples displayed the presence of particles or micro-pores dispersed along grain boundaries and within each grain. The presence of such a large number of post-HIP inclusions was also observed by Irukuvarghula *et al.* [36], who hypothesized that they form during HIP due to the fracture of residual oxide films from SLM, taking on specific geometry to minimize surface energy between the metal and oxide layer.

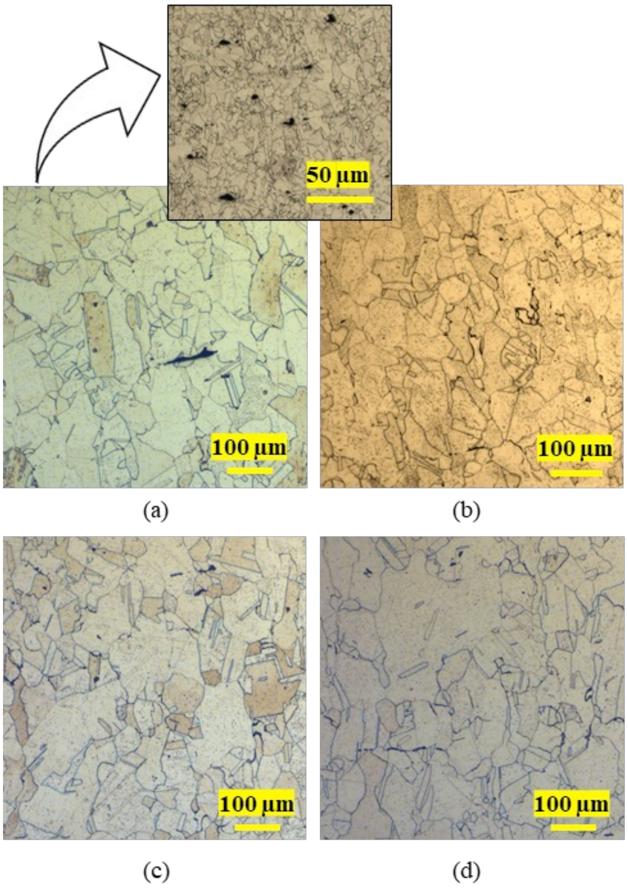

(a) (b)

(c) (d)

Fig 13 Microstructures of samples after HIP at **a** 50 bar, **b** 1050 bar, **c** 1500 bar and **d** 2000 bar

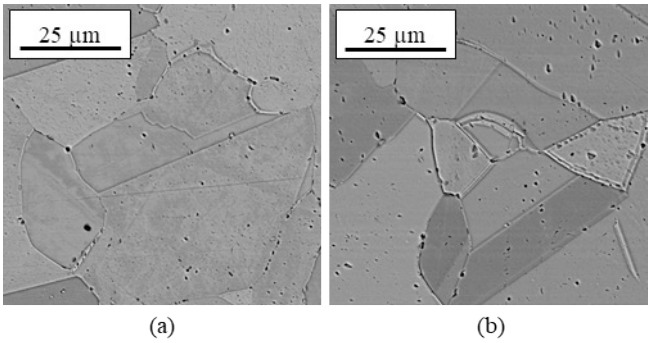

(a) (b)

Fig 14 SEM images of samples after HIP at **a** 50 bar and **b** 1050 bar

A line EDS measurement was performed over one of these particles (Fig. 15), highlighting increases in Si, O and Mn compared to the matrix (Table 8). Such inclusions therefore form as a result of a chemical reaction between elements already present in the matrix (Si and Mn) and residual oxygen present within the build chamber.

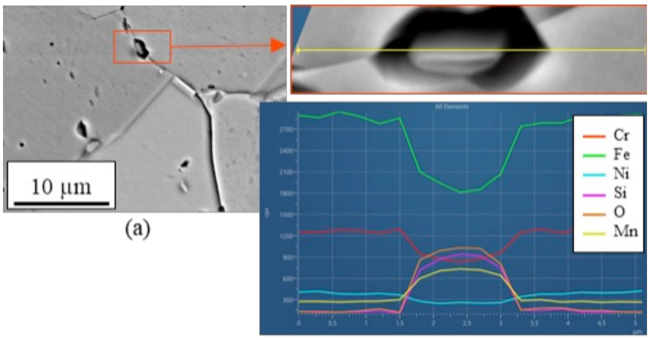

(a)

(b)

Fig 15 a EDS line scan performed on an inclusion found within a sample subject to HIP at 1050 bar and **b** corresponding elemental quantities identified during analysis

In contrast to the explanation given by Irukuvarghula *et al.* [36], the present authors believe that this outcome is due to gas (nitrogen and residual oxygen) remaining entrapped within the component during SLM and subsequently dissolving within the matrix and reacting with other elements when subject to high temperatures. Performing HIP on components produced by SLM can therefore close pores containing gas in the as-built state but cause the formation of non-metallic inclusions. The fact that the majority of dark areas within the SEM image appear empty is probably due to the ejection of inclusions during polishing of metallographic samples.

Other selected inclusions were also analyzed with EDS. Figure 16 shows inclusions found in samples subject to various post-processing conditions. These include HIP at 1050 bar followed by solubilization (Fig. 16a), HIP at 50 bar (Fig. 16b) and solubilization only (Fig. 16c). The corresponding EDS spectra are provided in Table 9. The atomic percentage appears to indicate silicate inclusions from the olivine family $(Mn,Fe)_2Si_4$ for samples subject to HIP, while the ratio of oxygen to silicon for solubilized samples is closer to 3:1. *Yan et al.* [37,38] reported finding rhodonite ($MnSiO_3$) inclusions in austenitic stainless steel components produced with AM processes. Though the presence of this metastable state is justified by the high solidification rate typical of SLM, the dimensions of crystals in the aforementioned study are in the order of nanometers (15-100 nm) while the inclusions in Fig. 16 are in the order of a few microns.

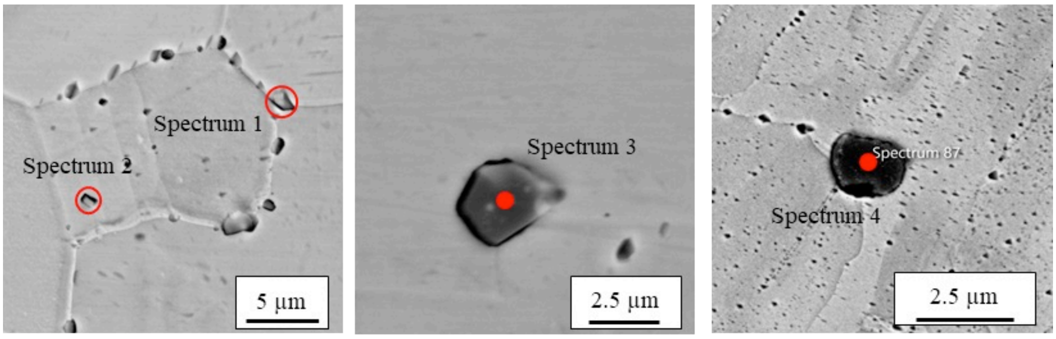

(a)

(b)

(c)

Fig 16 EDS analysis of inclusions from **a** a sample subject to HIP at 1050 bar followed by solubilization, **b** a sample subject to HIP at 50 bar and **c** a sample subject to solubilization only

Table 9 EDS spectra of inclusions found in HIP and solubilized samples (refer to Fig. 15) [wt.%/ at.%]

wt.% / at.%	O		Cr		Mn		Si		Mo		Ni		Fe
Spectrum 1	12.04	32.86	13.98	11.74	7.56	6.01	4.93	7.66	2.13	0.97	8.01	5.96	Bal.
Spectrum 2	19.98	45.60	11.27	7.91	12.38	8.23	8.59	11.17	1.24	0.47	6.4	9.98	
Spectrum 3	31	57.97	10.05	5.73	29.74	16.20	15.27	16.27	/		0.97	0.50	
Spectrum 4	31.88	55.99	10.82	5.85	36.66	18.75	17.41	17.41	0.20	0.06	0.30	0.14	

Other types of non-metallic inclusions were also identified in HIP samples (Fig. 17), but none were found with the same frequency as those described above.

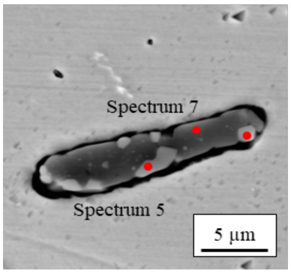

wt. %	O	Cr	Mn	Si	Mo	Ni	Al	Ca	Fe
Spectrum 5	33.55	5.12	31.61	18.85	-	0.39	0.34	2.09	Bal.
Spectrum 6	28.78	32.3	23.49	3.57	-	0.34	3.57	0.42	Bal.
Spectrum 7	28.84	19.9	22.55	8.05	0.42	1.51	2.44	0.98	Bal.

Fig. 17 Inclusions present in a sample subject to HIP at 1050 bar followed by solubilization and corresponding EDS spectra of the resulting elements [wt. %]

4. Discussion

Experiments performed within this work had the aim of investigating the mechanical properties and microstructure of AISI 316L components produced by SLM and subject to various post-processing procedures. The DT phase of the investigation focused on the link between HIP post-processing results and the initial density of SLM components. For low-density components (approximately 94 %), HIP increased the density by up to 1 % but was unable to achieve acceptable values, even at the highest tested pressure (2000 bar), see Fig. 3. This behavior is in general agreement with results in the literature relating to HIP performed on cast components [26-28], as previously discussed. It can therefore be concluded that the introduction of HIP after SLM is of little benefit if the as-built component is produced without SLM process optimization. On the contrary, if HIP is utilized for post-processing of high-density SLM components, it is possible to achieve final density values very close to 100 %.

Having ascertained this outcome, it was necessary to better understand the effect that such an increase in density could have on the mechanical properties of a component, noting that HIP introduces a non-trivial thermal cycle. Alongside these conditions, a solubilization heat treatment was also performed at a temperature only slightly below that at which HIP was performed, 1050 °C instead of 1150 °C. This additional experiment provided not only more data, but also the possibility of obtaining an intermediate condition between as-built specimens and HIP post-processing to allow a first approximation to be made as to the relative influence of HIP pressure and thermal cycle on the resulting outcome.

As-built samples exhibited higher yield strength (by approximately 45 %) and lower elongation (up to 53 % lower for HIP at 1050 bar) due to the sub-grain texture acting as a barrier to dislocation movement. This consideration is in alignment with the observed stress-strain behavior (Fig. 8), which displayed an absence of strain hardening for as-built samples. The lower ductility of as-built samples was confirmed with hardness measurements, where it was found that as-built samples had highest hardness (approximately 240 HV), while those subject to HIP had lowest hardness (approximately 160 HV), as show in Table 7.

These outcomes were also confirmed by analyzing samples subject to the solubilization heat treatment only. In this case, the yield strength was lower than the as-built samples by 24 % due to the disappearance of micro-cells during the imposed thermal cycle, but still higher than HIP samples by approximately 27 % due to incomplete recrystallization. Solubilization increased the ductility of as-built samples from 33.1 % to 44.7 %, but less so than components subject to HIP (70.9 %) for the same reasons (Figs. 7 and 8).

Finally, detailed SEM analysis of the resulting microstructures revealed the presence of numerous non-metallic inclusions with chemical compositions in line with $(Mn,Fe)_2SiO_4$ and $MnSiO_3$, both at grain edges and internally (see Figs. 15-17). Further investigation into this aspect is required to confirm the presence and types of inclusions. These were evident in both samples subject to HIP as well as those subject to solubilization only. This outcome suggests that the formation of inclusions is due to temperature and not pressure, with the latter only applied during HIP. A greater number of defects and micro-pores was nonetheless evident in samples subject to solubilization only compared to HIP-treated samples, confirming the validity of HIP in removing a large proportion of porosity.

5. Conclusion

The aim of this study was to investigate the influence of different post-processing conditions on the mechanical properties, hardness and microstructure of AISI316L components manufactured by SLM. By performing HIP and a solubilization heat treatment, the following key results were found:

1. HIP post-processing, even at elevated pressures (up to 2000 bar), produces defect-free components only when the initial density is high. Acceptable results were not achieved when the initial density was 94 %, while values very close to 100 % were achieved when the initial density was at least 99 %;
2. SLM process parameters must therefore be optimized in all cases if porosity is to be eliminated;
3. HIP pressures in the order of 50 bar do not have any significant impact on porosity, while pressures of 1050 bar or above produce final results that approach 100 % density;
4. Performing HIP implies complete recrystallization of grains obtained during SLM and therefore increased ductility at the expensive of yield strength and hardness;
5. Solubilization heat treatment after SLM only partially modifies the microstructure, for which the percentage elongation and yield strength of samples subject to this treatment

take on intermediate values. Where the same treatment is instead performed after HIP, there are no direct consequences on the mechanical properties;

6. SEM analysis of samples subject to post-processing reveals the presence of numerous non-metallic inclusions. This observation can be accounted for by considering the reaction of residual oxygen trapped within pores in the base material at high temperature.

References

[1] González-Henríquez CM, Sarabia-Vallejos MA, Rodriguez-Hernandez J (2019) Polymers for additive manufacturing and 4D-printing: Materials, methodologies, and biomedical applications. Progress in Polymer Science 94:57-116. https://doi.org/10.1016/j.progpolymsci.2019.03.001

[2] Liu S, Shin YC (2019) Additive manufacturing of Ti6Al4V alloy: A review. Materials & Design 164:107552. https://doi.org/10.1016/j.matdes.2018.107552

[3] Harun WSW, Kamariah MSIN, Muhamad N, Ghani SAC, Ahmad F, Mohamed Z (2018) A review of powder additive manufacturing processes for metallic biomaterials. Powder Technology 327:128-151. https://doi.org/10.1016/j.powtec.2017.12.058

[4] Kurzynowsy T, Gruber K, Dtopyra W, Kuznicka B, Chlebus E (2018) Correlation between process parameters, microstructure and properties of 316 L stainless steel processed by selective laser melting. Materials Science and Engineering: A 718:64-73. https://doi.org/10.1016/j.msea.2018.01.103

[5] Fortunato A, Lulay A, Melkote S, Liverani E, Ascari A, Umbrello D (2018) Milling of maraging steel components produced by selective laser melting. The International Journal of Advanced Manufacturing Technology 94:1895-1902. https://doi.org/10.1007/s00170-017-0922-9

[6] Zhang J, Song B, Wei Q, Bourell D, Shi Y (2019) A review of selective laser melting of aluminum alloys: Processing, microstructure, property and developing trends. Journal of Materials Science & Technology 35:270-284. https://doi.org/10.1016/j.jmst.2018.09.004

[7] Fayazfar H, Salarian M, Rogalsky A, Sarker D, Russo P, Paserin V, Toyserkani E (2018) A critical review of powder-based additive manufacturing of ferrous alloys: Process parameters, microstructure and mechanical properties. Materials and Design 144:98-128. https://doi.org/10.1016/j.matdes.2018.02.018

[8] Liverani E, Toschi S, Ceschini L, Fortunato A (2017) Effect of Selective Laser Melting (SLM) process parameters on microstructure and mechanical properties of 316L austenitic stainless steel. Journal of Materials Processing Technology 249:255-263. https://doi.org/10.1016/j.jmatprotec.2017.05.042

[9] Wang Z, Xiao Z, Tse Y, Huang C, Zhang W (2019) Optimization of processing parameters and establishment of a relationship between microstructure and mechanical properties of SLM titanium alloy. Optics & Laser Technology 112:159-167. https://doi.org/10.1016/j.optlastec.2018.11.014

[10] Hack H, Link R, Knudsen E, Baker B, Olig S (2017) Mechanical properties of additive manufactured nickel alloy 625. Additive Manufacturing 14:105-115. https://doi.org/10.1016/j.addma.2017.02.004

[11] Benedetti M, Fontanari V, Bandini M, Zanini F, Carmignato S (2018) Low-and high-cycle fatigue resistance of Ti-6Al-4V ELI additively manufactured via selective laser melting: Mean stress and defect sensitivity. International Journal of Fatigue 107:96-109. https://doi.org/10.1016/j.ijfatigue.2017.10.021

[12] Fotovvati B, Namdari N, Dehghanghadikolaei A (2018) Fatigue performance of selective laser melted Ti6Al4V components: State of the art. Materials Research Express 6(1):012002. https://doi.org/10.1088/2053-1591/aae10e

[13] Rafi HK, Starr TL, Stucker BE (2013) A comparison of the tensile, fatigue, and fracture behavior of Ti-6Al-4V and 15-5 PH stainless steel parts made by selective laser melting. The International Journal of Advanced Manufacturing Technology 69(5-8):1299-1309. https://doi.org/10.1007/s00170-013-5106-7

[14] Dörfert R, Zhang J, Clausen B, Freiße H, Schumacher J, Vollertsen F (2019) Comparison of the fatigue strength between additively and conventionally fabricated tool steel 1.2344. Additive Manufacturing 27:217-223. https://doi.org/10.1016/j.addma.2019.01.010

[15] Carneiro L, Jalalahmadi B, Ashtekar A, Jiang Y (2019) Cyclic deformation and fatigue behavior of additively manufactured 17–4 PH stainless steel. International Journal of Fatigue 123:22-30. https://doi.org/10.1016/j.ijfatigue.2019.02.006

[16] Sun Y, Moroz A, Alrbaey K (2014) Sliding wear characteristics and corrosion behaviour of selective laser melted 316L stainless steel. Journal of Materials Engineering and Performance 23:518-526. https://doi.org/10.1007/s11665-013-0784-8

[17] Yasa E, Kruth JP (2011) Microstructural investigation of Selective Laser Melting 316L stainless steel parts exposed to laser re-melting. Procedia Engineering 19:389-395. https://doi.org/10.1016/j.proeng.2011.11.130

[18] Wei K, Lv M, Zeng X, Xiao Z, Huang G, Liu M, Deng J (2019) Effect of laser remelting on deposition quality, residual stress, microstructure, and mechanical property of selective laser melting processed Ti-5Al-2.5Sn alloy. Materials Characterization 150:67-77. https://doi.org/10.1016/j.matchar.2019.02.010

[19] Atkinson HV, Davies S (2000) Fundamental aspects of hot isostatic pressing: An overview. Metallurgical and Materials Transactions A 31:2981-3000. https://doi.org/10.1007/s11661-000-0078-2

[20] Kreitcberg A, Brailovski V, Turenne S (2017) Effect of heat treatment and hot isostatic pressing on the microstructure and mechanical properties of Inconel 625 alloy processed by laser powder bed fusion. Materials Science and Engineering 689:1-10. https://doi.org/10.1016/j.msea.2017.02.038

[21] Tillmann W, Schaak C, Nellesen J, Schaper M, Aydinöz ME, Hoyer KP (2017) Hot isostatic pressing of IN718 components manufactured by selective laser melting. Additive Manufacturing 13:93-102. https://doi.org/10.1016/j.addma.2016.11.006

[22] Li P, Warner DH, Pegues JW, Shamsaei V, Roach MD, Phan N (2019) Investigation of the mechanisms by which hot isostatic pressing improves the fatigue performance of powder bed fused Ti-6Al-4V. International Journal of Fatigue 120:342-352. https://doi.org/10.1016/j.ijfatigue.2018.10.015

[23] Molaei R, Fatemi A, Phan N (2018) Significance of hot isostatic pressing (HIP) on multiaxial deformation and fatigue behaviors of additive manufactured Ti-6Al-4V including build orientation and surface roughness effects. International Journal of Fatigue 117:352-370. https://doi.org/10.1016/j.ijfatigue.2018.07.035

[24] Lavery NP, Cherry J, Mehmood S, Davies H, Girling B, Sackett E, Brown SGR, Sienz J (2017) Effects of hot isostatic pressing on the elastic modulus and tensile properties of 316L parts made by powder bed laser fusion. Materials Science and Engineering: A 693:186-213. https://doi.org/10.1016/j.msea.2017.03.100

[25] Röttger A, Geenen K, Windmann M, Binner F, Theisen W (2016) Comparison of microstructure and mechanical properties of 316 L austenitic steel processed by selective laser melting with hot-isostatic pressed and cast material. Materials Science and Engineering A 678:365–376. https://doi.org/10.1016/j.msea.2016.10.012

[26] Hafenstein S, Werner E (2019) Pressure dependence of age-hardenability of aluminum cast alloys and coarsening of precipitates during hot isostatic pressing. Materials Science and Engineering: A 757:62-69. https://doi.org/10.1016/j.msea.2019.04.077

[27] Li J, Yuan C, Guo J, Hou J, Zhou L (2014) Effect of hot isostatic pressing on microstructure of cast gas-turbine vanes of K452 alloy. Progress in Natural Science: Materials International 24:631-636. https://doi.org/10.1016/j.pnsc.2014.10.008

[28] Islam MA, Farha ZN (2011) The influence of porosity and hot isostatic pressing treatment on wear characteristics of cast and P/M aluminum alloys. Wear 271:1594-1601. https://doi.org/10.1016/j.wear.2011.01.037

[29] Samal PK, Newkirk JW (2015) ASM Handbook, Volume 7: Powder Metallurgy. ASM International, United States.

[30] AISI type 316L stainless steel, annealed and cold drawn bar. Matweb. http://matweb.com/search/DataSheet.aspx?MatGUID=c02b8c0ae42e459a872553e0ebfab648&ckck=1. Accessed 02 October 2019.

[31] Yadollahi A, Sjamsaei N, Thompson SM, Seely DW (2015) Effects of process time interval and heat treatment on the mechanical and microstructural properties of direct laser deposited 316L stainless steel. Mater. Sci. Eng. A 644:171–183. https://doi.org/10.1016/j.msea.2015.07.056

[32] Murr LE (2018) A metallographic review of 3D printing/additive manufacturing of metal and alloy products and components. Metallography, Microstructure and Analysis 7:103–132. https://doi.org/10.1007/s13632-018-0433-6

[33] Zhong Y, Liu L, Wikman S, Cui D, Shen Z (2016) Intragranular cellular segregation network structure strengthening 316L stainless steel prepared by selective laser melting. Journal of Nuclear Materials 470:170-178. https://doi.org/10.1016/j.jnucmat.2015.12.034

[34] Krakhmalev P, Fredriksson G, Svensson K, Yadroitsev I, Yadroitsava I, Thuvander M, Peng R (2018) Microstructure, solidification texture, and thermal stability of 316 L stainless steel manufactured by laser powder bed fusion. Metals 8:643. https://doi.org/10.3390/met8080643

[35] Saeidi K, Gao X, Shen ZJ, Lofaj F, Kvetková L (2015) Transformation of austenite to duplex austenite-ferrite assembly in annealed stainless steel 316L consolidated by laser melting. Journal of Alloys and Compounds 633:463-469. https://doi.org/10.1016/j.jallcom.2015.01.249

[36] Irukuvarghula S, Hassanin H, Cayron C, Aristizabal M, Attallah MM, Preuss M (2019) Effect of powder characteristics and oxygen content on modifications to the microstructural topology during hot isostatic pressing of an austenitic steel. Acta Materialia 172:6-17. https://doi.org/10.1016/j.actamat.2019.03.038

[37] Yan F, Xiong W, Faierson EJ (2017) Grain structure control of additively manufactured metallic materials. Materials 10:1260. https://doi.org/10.3390/ma10111260

[38] Yan F, Xiong W, Faierson E, Olson GB (2018) Characterization of nano-scale oxides in austenitic stainless steel processed by powder bed fusion. Scripta Materialia 155:104-108. https://doi.org/10.1016/j.scriptamat.2018.06.011